[Ludovica Casnedi, Marta Cappai, Alberto Cincotti, Francesco Delogu, Giorgio Pia, Porosity effects on water vapour permeability in earthen materials: Experimental evidence and modelling description, Journal of Building Engineering, 27, January, 2020, pagg. 100987]

https://doi.org/10.1016/j.jobe.2019.100987

Porosity effects on water vapour permeability in earthen materials:

Experimental evidence and modelling description

Ludovica Casnedi, Marta Cappai, Alberto Cincotti, Francesco Delogu, Giorgio Pia*

Dipartimento di Ingegneria Meccanica, Chimica e dei Materiali, Università degli Studi di Cagliari, via Marengo 2, 09123 Cagliari, Italy

* Corresponding author: giorgio.pia@dimcm.unica.it, tel. +39 070 675 50 51, fax +39 070 675 50 67

Abstract

This work focuses on the relationship between water vapour permeability and porosity in earthen materials. Earth blocks have been suitably fabricated and their pore size distribution evaluated along with water vapour permeability. Experimental results are compared with theoretical predictions obtained from a fractal model relating porosity to transport processes. Experimental and modelling outcomes compare remarkably well, thus making the fractal model show promise for addressing the design of earth materials with tailored properties.

Keywords: Earth materials; Porous materials; Water vapour permeability; Model predictions.

Introduction

Earth has been used as a building material since the dawn of times. Dating back approximately to 8300 BC and eternalized in the Bible story of the first Israelitic conquest in the land of Canaan, the walls of Jericho probably represent the most famous and magnificent example in this respect [1]. However, it is only one of the about 220 World Heritage sites involving earth buildings mentioned in the UNESCO's World Heritage List, approximately the 20% of the total [2]. The fact that about 50% of world population still lives in earth structures makes it clear that the importance of earthen materials is not consigned to the past [3].

Although earth-based constructions are commonly associated with less industrialized countries, most advanced societies are witnessing a remarkable surge in interest in earth and its application in buildings. Not only earth is an inexpensive raw material that enables simple *in situ* production processes [4], but also it exhibits a wide spectrum of advantageous properties that make it non-toxic, non-polluting and able to spontaneously contribute to temperature and moisture control in buildings. The latter properties are particularly relevant in the light of the harmful effects that humid environments can have on human health [5] and the damage they can cause to the building itself in terms of accelerated aging [6–8].

Material damage stems from a vast range of processes triggered by freeze-thaw cycles in the presence of liquid water or water vapour in the accessible pores of porous materials. Sub-surface salt crystallization, dissolution of mineral phases and chemical reactions can readily affect the mechanical stability of building blocks [7]. Innovative design of building materials has been often invoked as the optimal solution strategy to enhance material performances and reduce undesired moisture effects. Within this framework, attention has generally focused on the development of modelling approaches that could suitably relate material structure to water vapour permeability. While various models have been proposed to generically account for the flow of gases and vapours in several porous materials [9–14], the relationship between the structure of porous materials and their permeability to gases and vapours remains an open question.

In this respect, the use of fractal geometry to describe the structural features related to porosity distribution shows considerable promise. With their inherent complexity and self-similarity, fractals allow reproducing to a considerable extent irregular profiles and structures with non-integer dimension [15,16]. Literature on porous materials already includes a few examples of fractal models [17,18]. In particular, the fractal geometry has been shown to enable predictions on gas and vapour permeability [19], also covering hygroscopic and over-hygroscopic ranges [20], on the distribution of fracture lengths and pores [21,22], and on gas diffusion [23]. The capability of fractal geometry of capturing the fundamental aspects of porous materials also emerges from the systematic studies addressing spontaneous permeation in natural and artificial matrices taking into account shape, size and tortuosity of pores [19,24].

On completion of this wide overview on fractal geometry and porous media, it is needed to note that it is necessary to have modelling approaches capable of reproducing microstructure features for generalising an analytical procedure. For this reason, a new fractal phenomenological model, usually called Intermingled Fractal Units' model (IFU model), has been proposed recently with the aim of predicting different physical characteristics of porous materials such as sorptivity, permeability, heat transfer and mechanical properties [25–28]. It is constructed considering different fractal figures and non-porous parts mixed together for reproducing representative structures of fractal or non-fractal porous materials, which have very similar pore size distribution and pore volume fraction [28,29]. After having verified the real correspondence between material microstructure and model reconstruction, analytical procedure could be applied for predicting different physical phenomena. The easy formalisation of this model, which is based on porosimetric experimental data, allows obtaining a procedure without considering empirical constants.

In this work, we focus on the flow of water vapour through accessible porosity of earth materials. To this aim, experiments of water vapour permeability have been performed on suitably fabricated earthen blocks. The obtained results are compared with the predictions obtained by the model based on intermingled fractal units, which reproduces the pore size distribution obtained by Hg intrusion porosimetry. It is shown that model predictions compare remarkably well with experimental estimates.

A consolidate use of this fractal modelling may only be achieved by verifying the reliability of the procedure adopted. For this reason, in previous works, different materials have been modelled by using the Intermingled Fractal Units' model with the aim of predicting mechanical, thermal and fluid flow behaviour [25–28]. However, the remarkable aim of this fractal model is to formalise a software for designing and controlling porous building materials by predicting simultaneously their different performances. In addition, this fractal model can also be used for estimating decay and weathering state resulting from porous structure modification during their useful life. Although different models have been reported in literature, the relevant and novel purpose of the Intermingled Fractal Units' model is its capacity to be applied for studying different porous materials. Overall, the proposed paper represents a step forward in this direction.

Materials and methods

Experiments were performed on earth-based products consisting of mixtures of earth, water, sand and straw available in the area of *Medio Campidano* in Sardinia. Four different compositions, corresponding to samples hereafter referred to as E1, E2, E3 and E4, were explored. Relevant data are summarized in Tab. 1.

Raw materials were characterized by thermogravimetric and X-ray diffraction analyses using, respectively, a TA TGA 5500 apparatus and a Rigaku Miniflex II diffractometer equipped with monochromatic Cu K_α radiation.

Earth-based products were cured for 3 months under ambient conditions characterized by temperature and humidity in the ranges between 20 and 23 °C and between 40 and 50% respectively. Then, cured samples were subjected to Hg intrusion porosimetry to evaluate the pore size distribution. A Micrometrics AutoPoreIV porosimeter at a working pressure of about 2000 bar was used. Water vapour permeability was measured carrying out experiments according to UNI EN 15803 (UNI EN 15803) on cylinders 13 cm in diameter and 2 cm in height suitably cut from parent 40×20×10 cm^3 blocks. Although prescriptions suggest using at least 3 samples, investigation was performed on 10 samples. Cylinders were placed inside a pre-conditioned test chamber and suitably oriented to have bases perpendicular to the flow direction of water vapour. The time required to attain equilibrium conditions depends on the sample height, L_0. While a base was exposed to a desiccant, the other was exposed to ambient conditions. Internal and external relative humidity, RH_{int} and RH_{ext} respectively, were set equal to about 2% and 50 ± 3%. Cylinder weight changes, Δm, were evaluated at regular time intervals, Δt.

The amount of water vapour flown in the samples, Q_{exp}, was estimated by the slope of the plot of Δm as a function of Δt. Then, the density of water vapour flow, V_{exp}, was calculated dividing Q_{exp} by the base area of the samples. Water vapour permeability was calculated according to the expression

$$\delta_{\text{exp}} = \frac{V_{\text{exp}} L_0}{\Delta p}, \qquad (1)$$

where Δp is the pressure difference between the two opposite bases of the cylindrical samples. In particular, Δp appearing in Equation (1) was related to RH by means of the equilibrium vapor pressure of water $P^*_{H_2O}(T)$ measured at 23 °C, i.e. $\Delta p = P^*_{H_2O}(T)(RH_{ext} - RH_{int})$, with $P^*_{H_2O}(23\ °C)$ = 2813.102 Pa.

Fractal model

The model involves the combination of different units consisting of Sierpinski carpets with different characteristic lengths. The Sierpinski carpet is one of the most famous fractal objects. It is obtained dividing a square of side *l* by a factor *F* into equal sub-squares. At first iteration, a selected number of sub-squares is removed, thus creating square voids. All the structural units have the same characteristic length

$$\lambda_{\max} = \frac{l}{F} . \tag{2}$$

The fractal object is constructed by repeating indefinitely the iteration process. The size of voids at the *n*-th iteration is equal to

$$\lambda_{n^{th}} = \frac{l}{F^{n}} = \frac{\lambda_{\max}}{F^{(n-1)}} . \tag{3}$$

The fractal dimension of the Sierpinski carpet, D_f, is calculated as a function of the number of sub-squares not removed at the first iteration, N_{RSQ}, and the factor *F*. Accordingly,

$$D_f = \frac{\log(N_{RSQ})}{\log(F)} . \tag{4}$$

The non-integer dimension stems from the inherent porosity of the fractal construction, characterized by removed sub-squares with side λ_i between $\lambda_{\max}$ and $\lambda_{\min}$, perimeter of removed sub-squares equal to 4 λ, porosity equal to the ratio between void and solid volume fractions and monotonic pore size distribution.

The two-dimensional Sierpinski carpet can be used to construct an ideal three-dimensional porous material assuming that its cross-sections invariably consist of the same Sierpinski carpet used as the mathematical basis. However, it is here worth noting that the structural features mentioned above preclude the use of Sierpinski carpet for a satisfactory description of real porous materials, which typically have non-monotonic pore size distribution. Nevertheless, such objective can be profitably pursued by suitably modifying the construction of the Sierpinski carpet. In particular, remarkable results can be obtained by leaving a certain number of sub-squares unaffected by the space carving process associated with the generation of the fractal. As shown in Fig. 1, this choice translates into sub-squares remaining solid throughout the iteration process. The combination of structural units with a different degree of porosity finally results in a modified Sierpinski carpet that can be used to model porous architectures.

To such aim, different modified Sierpinski carpets can be properly mixed. Let us consider, for instance, two structural units *A* and *B* with different characteristic lengths. For both units, space carving can be specifically tailored to obtain different total porosity and void size distribution.

Let us combine n_B *B* units for every *A* unit. The result is a fractal object that can be used to construct a realistic three-dimensional porous material. For this material, the model predicts a total porosity degree equal to $\varepsilon_{mod} = (A_{Ap} + n_B \cdot A_{Bp})/(A_A + n_B \cdot A_B)$, where A_A, A_B, A_{Ap} and A_{Bp} are the total areas and the total pore areas of *A* and *B* units respectively. If ε_{mod} is set equal to the porosity degree measured experimentally, ε_{exp}, the number of *B* units per *A* unit can be readily calculated from the expression

$$n_B = (A_{Ap} - \varepsilon_{\exp} \cdot A_A) \big/ (\varepsilon_{\exp} \cdot A_B - A_{Bp}) . \qquad (5)$$

Geometrical construction of fractal model is obtained by using random arrangement of B units around A unit. This configuration could casually change section per section in 3D extrusion. In this sense, it is also worth noting that we can confidently associate tortuosity to individual pores. Indeed, the model only requires that any cross-section of the porous material corresponds to the two-dimensional modified Sierpinski carpet chosen as construction unit. Therefore, there is no need to look at pores as at straight channels. Therefore, the model allows tortuosity as an additional parameter.

Due to its capability of accurately describing experimental pore size distributions, the model can be used to predict water vapour permeability, δ. This quantity depends on both overall porosity degree and pore size distribution. Indeed, a fluid flows at higher rates in larger pores.

Let us consider a structural unit consisting of a Sierpinski carpet with number of pores

$$N_{pores(i=n)} = F^{i \cdot D_f} (F^{2-D_f} - 1) . \qquad (6)$$

According to literature [31], three different mechanisms contribute to water vapour permeability in earth-based blocks, namely gas bulk viscous flow (laminar flow), gas diffusion (continuum and Knudsen) and surface diffusion. Following the analogy with resistances in electric circuits [32], continuum and Knudsen gas diffusions are modelled as resistances in series combined in parallel with gas viscous flow (Hagen-Poiseuille) and surface diffusion. The contribution of each mechanism is evaluated taking into account any morphological feature underlying porosity, including pore size distribution, tortuosity and interconnectivity.

Usually, continuum diffusion in the gaseous phase is neglected. The reason lies in the evidence that, in small pores, Knudsen flow exhibits the higher flow resistance, thus representing the rate-limiting step. In contrast, in large pores diffusion flow is definitely less important than laminar flow in the bulk of the gas phase. Concerning surface diffusion, it can really affect the transport process only when pores are very small [33]. In particular, literature suggests that surface diffusion can play a non-negligible role for pore sizes smaller than 1 nm [32]. Therefore, it can be neglected in the case of the earth-based materials investigated in the present work, which exhibit pore size between 0.03 and 100 μm.

If continuum diffusion in gas phase and surface diffusion are neglected [34,35], only Hagen-Poisseuille flow and Knudsen diffusion mechanisms give contribution. Accordingly, the volumetric rate for a single pore can be expressed as

$$q(\lambda) = \frac{\pi}{128} \frac{\Delta p}{L_t(\lambda)} \frac{\lambda^4}{\mu} + \frac{\lambda^3}{12 L_t(\lambda)} \frac{\Delta p}{p} \sqrt{\frac{8\pi RT}{M}} \,, \tag{7}$$

where Δp, L_t, λ, μ, p, M and R are, respectively, the pressure loss, the tortuous capillary length, the pore diameter, the dynamic viscosity, the mean partial pressure of gas or vapour diffusion, the molecular weight of gas molecules and the universal gas constant.

The ratio between the mean free path of molecules, τ, and the pore size, λ, defines the so-called Knudsen number, *Kn*. When *Kn* is smaller than 0.01, the collisions between vapour molecules are more probable than between molecules and pore walls. Vice versa, when *Kn* is larger than 10, collisions between molecules and pore walls dominate. In the former case, a viscous Hagen-Poiseuille flow occurs, while Knudsen diffusion is said to occur in the latter. For *Kn* values between 0.01 and 10, the two mechanisms coexist [7].

The length of tortuous pores, L_t, of size λ can be expressed as [36,37]

$$L_t(\lambda) = L_0^{D_T} \lambda^{1-D_T} \,, \tag{8}$$

where L_0 is the projection of the pore length on the sample axis and

$$\mathrm{D_T} = 1 + \frac{\ln \tau_{\mathrm{class}}}{\ln\left(\frac{\mathrm{L_0}}{\lambda}\right)} \tag{9}$$

is the fractal dimension of tortuosity [38]. The tortuosity of a specific class of capillaries, τ_{class}, is [39]

$$\tau_{\mathrm{class}} = 1 + a \ln \frac{1}{\varepsilon_{class}} \,, \tag{10}$$

where ε_{class} is the porosity fraction ascribable to the specific pore class and a is a constant equal to 0.63 that accounts for the pore shape [40–42].

Based on Eq. 6, Eq. 7 can be rewritten as

$$q_{pore}(\lambda) = \frac{\pi}{128}\frac{\Delta p}{L_t(\lambda)}\frac{1}{\mu}\frac{\lambda_{\max}^4}{F^{4(i-1)}} + \frac{\lambda_{\max}^3}{12F^{3(i-1)}L_t(\lambda)}\sqrt{\frac{8\pi RT}{M}}\frac{\Delta p}{p}\,. \tag{11}$$

If the number of pores for a specific class is taken into account, the fluid flow across the pores is

$$Q_{class} = \left(\frac{\pi}{128}\frac{\Delta p}{L_t(\lambda)}\frac{1}{\mu}\frac{(\lambda_{\max})^4}{F^{4(i-1)}} + \frac{\lambda_{\max}^3}{12F^{3(i-1)}L_t(\lambda)}\sqrt{\frac{8\pi RT}{M}}\frac{\Delta p}{p}\right)\cdot\left[F^{i\bullet D_f}\left(F^{2-D_f}-1\right)\right]. \tag{12}$$

Therefore, when the entire pore size distribution is considered, the total fluid flow across one of the fractal units utilized for describing the sample structure is equal to

$$Q_{BU} = \sum_{i=n}^{i_{\max}}\left\{\left(\frac{\pi}{128}\frac{\Delta p}{L_t(\lambda)}\frac{1}{\mu}\frac{(\lambda_{\max})^4}{F^{4(i-1)}} + \frac{\lambda_{\max}^3}{12F^{3(i-1)}L_t(\lambda)}\sqrt{\frac{8\pi RT}{M}}\frac{\Delta p}{p}\right)\cdot\left[F^{i\bullet D_f}\left(F^{2-D_f}-1\right)\right]\right\}. \tag{13}$$

Eq. 13 allows expressing the density of water vapour flow as

$$V_{BU} = \frac{1}{A}\sum_{i=n}^{i_{\max}}\left\{\left(\frac{\pi}{128}\frac{\Delta p}{L_t(\lambda)}\frac{1}{\mu}\frac{(\lambda_{\max})^4}{F^{4(i-1)}} + \frac{\lambda_{\max}^3}{12F^{3(i-1)}L_t(\lambda)}\sqrt{\frac{8\pi RT}{M}}\frac{\Delta p}{p}\right)\cdot\left[F^{i\bullet D_f}\left(F^{2-D_f}-1\right)\right]\right\}. \tag{14}$$

Finally, it is possible to re-write Eq. 1 as

$$\delta_{IFU} = \frac{L_0\sum V_{BU}}{\Delta p}\,, \tag{15}$$

where the sum extends over the different fractal units used to account for the sample structure.

Although the model describes only monodimensional fluid flow, it provides information on all of those materials with a percolating architecture and for all of those processes with a preferential direction [43–45].

This approach, schematised in Fig. 2, is capable of representing any type of real porous microstructures. It consists of several steps: (a) experimental water vapour permeability measurement; (b) porosity tests for the measurement of a pore size distribution by mercury intrusion porosimetry; (c) intermingled Sierpinski carpets (contiguous units) for reproducing porous microstructure; (d) analytical procedure for calculating model water vapour permeability; (e) comparison between experimental and modelling data.

It is important to observe that every parameter which is expressed in several formulas reported above has physical sense. Non-empirical quantities have been considered. In particular, for the geometrical construction of the Intermingled Fractal Units' model, pore size, pore volume fraction, pore size range and tortuosity have values obtained by MIP. Fundamentally, results of MIP test have been used as input data for phenomenological reconstruction of porous microstructure (e.g. the number of units forming the model that is function of porosimetric data as reported in Eq. 5). In the analytical procedure, Δp, μ, p, M and R are physical quantities with specific values for proper water vapour experimental conditions (relative humidity, temperature, molecular flows, etc.).

Results and discussion

Earth materials investigated in this work exhibit the typical microstructure stemming from the aggregation of mineral particles with different shape and size. Mesostructure can be appreciated from SEM micrographs in Fig. 3. Self-similarity emerges from the comparison of structural features, which keep similar shape and size ratio on different length scales.

According to X-ray diffraction patterns such as the one shown in Fig. 4, earth materials comprise kaolinite, bytownite plagioclase and diopside pyroxene along with secondary smectite clay. Based on thermogravimetric analysis, the kaolinite and smectite clay contents are around 80% and 5% respectively. The relatively high clay content enhances chemical and thermal stability.

Data obtained by Hg intrusion porosimetry are shown in Fig. 5. It can be seen that experimental points arrange according to a monotonic decreasing trend. Different datasets approximately keep the same shape. However, the increase in the content of sand from E1 to E4 samples induces a corresponding increase of relatively large pores. Addition of sand to pristine material gives rise to new classes of pore size in the large pore region of the pore size distribution. The large pores simply correspond to the empty interstices between sand particles. According to literature [46], total porosity and pore size distribution suggest that materials belonging to the E1, E2, E3 and E4 series can exhibit, in principle, good performances with respect to thermal and hygroscopic responses to ambient conditions.

A few interesting features are summarized in Tab. 2. Pore size can be divided into three major intervals, namely P1 from 100 to 1.10 μm, P2 from 1.10 to 0.1 μm and P3 from 0.1 to 0.009 μm. It immediately appears that E2-1 and E3-1 samples have similar porosity and average pore radius, about 18% and 0.49 μm respectively, but different pore size distribution. Indeed, E2-1 samples have fewer pores in P1 and the E3-1 sample has fewer pores in P2. Along the same line, E1-1 and E4-1 samples have approximately the same pores in P2, about 11 %, but different total porosity, about 12.98% and

22.15% respectively, and different pores in P1, about 2.00% and 10.73 % respectively. For all samples, pores in P3 are minority.

The porosity features mentioned above have direct effect on the capacity of fluid transport. As shown in Fig. 6, water vapour is mostly absorbed during the early stages of permeation experiments, while saturation is attained after relatively long time. Experimental water vapour permeability and porosity correlate remarkably well. However, kinetics of permeation can be properly understood only referring to pore size distribution.

The water vapour permeability coefficients for E1, E2, E3 and E4 samples are equal to 0.44 ± 0.34, 1.98 ± 0.68, 4.38 ± 1.28 and 6.82 ± 1.26 kg m^{-1} s^{-1} Pa^{-1} respectively. The different structural features of E1, E2, E3 and E4 samples provide a rationale for the observed differences. The fractal model can suitably account for such differences provided that its fundamental parameters are properly chosen. Our choices are shown in Tab. 3. In this respect, it is worth noting that D_f, L_t, λ and L_0, R_{max} (the maximum pore ray), R_{min} (the minimum pore ray) and i are estimated from experimental data, while n is calculated using Eq. 5. The porosimetric curves in Fig. 5 clearly show that the model exhibits the capability of reproducing satisfactorily the pore size distributions determined from experimental measurements.

Calculated values of water vapour permeability are compared with experimental ones in Fig. 7. It can be seen that the agreement between modelling predictions and experimental data is fairly good. Thus, the fractal model exhibits a remarkable capability of faithfully representing the mesostructural features of the earth-based materials considered, simultaneously estimating correctly a crucial transport property such as water vapour permeability. This makes the fractal model a design tool for fabricating earth-based building blocks with properties tailored to application. The study of these materials by using the fractal model represents an innovation for different fields such as Cultural Heritage, in which diagnostics testes are limited to the impossibility to withdrawn a large quantity of material, and modern application in sustainable constructions in which it is a fundamental material design in order to obtain material's specific properties.

Conclusions

We fabricated earth-based materials with different mesostructures and subjected them to experimental tests aimed at evaluating water vapour permeability. Information on mesostructural features coming from experimental characterization was used to construct geometrical replicas of experimental systems. This was done using a fractal model able to relate mesostructure to transport properties. Once the model reproduced the mesostructural features evaluated experimentally, it was used to estimate water vapour permeability. The results obtained indicate that model predictions agree remarkably well with experimental findings. We conclude that the modelling approach developed shows significant promise for the description of real earth-based systems, also providing a valuable design tool to address fabrication methods and tailor structural and physical properties of earth-based materials. We also note that the fractal model can be readily extended to the description of classes of porous materials other from earth-based ones.

Acknowledgements

Financial support has been given by the University of Cagliari.

References

[1] M. Calkins, Materials for sustainable sites: a complete guide to the evaluation, selection, and use of sustainable construction materials. Wiley, New Jersey, 2009.

[2] D. Gandreau, L. Deboy, World Heritage, Inventory of earthen Architecture, UNESCO-sponsored programmes and publications, France 2012., (2012) 2012.

[3] R. Anger, L. Fontaine, R. Anger, L. Fontaine, Batir en terre, du grain de sable à l'architecture, Belin, Paris, 2009..pdf, 2009.

[4] E. Christoforou, A. Kylili, P.A. Fokaides, I. Ioannou, Cradle to site Life Cycle Assessment (LCA) of adobe bricks, J. Clean. Prod. 112 (2016) 443–452. doi:10.1016/j.jclepro.2015.09.016.

[5] Committee on Damp Indoor Spaces and Health Board on Health Promotion and Disease Prevention, Damp Indoor Spaces and Health. Chapter 5. Human Health Effects Associated with Damp Indoor Environments, National Academies Press, Washington, 2004.

[6] P.J. Annila, M. Hellemaa, T.A. Pakkala, J. Lahdensivu, J. Suonketo, M. Pentti, Extent of moisture and mould damage in structures of public buildings, Case Stud. Constr. Mater. 6 (2017) 103–108. doi:10.1016/j.cscm.2017.01.003.

[7] P.M. Bluyssen, Towards an integrative approach of improving indoor air quality, Build. Environ. 44 (2009) 1980–1989. doi:10.1016/j.buildenv.2009.01.012.

[8] S. You, W. Li, T. Ye, F. Hu, W. Zheng, Study on moisture condensation on the interior surface of buildings in high humidity climate, Build. Environ. 125 (2017) 39–48. doi:10.1016/j.buildenv.2017.08.041.

[9] R.M. Barrer, D.M. Grove, Flow of gases and vapours in a porous medium and its bearing on adsorption problems. Part I.-The steady state of flow, Trans. Faraday Soc. 47 (1951) 826–837. doi:10.1016/0042-207X(52)90247-9.

[10] R.W. Schofield, A.G. Fane, C.J.D. Fell, Gas and vapour transport through microporous membranes. II. Membrane distillation* 1, J. Memb. Sci. 53 (1990) 173–185. papers2://publication/uuid/5B4BDF46-EBEB-4FC5-B187-06F2082226FA.

[11] H. Baniasadi, A. Kamari, S. Heidararabi, A.H. Mohammadi, A. Hemmati-Sarapardeh, Rapid method for the determination of solution gas-oil ratios of petroleum reservoir fluids, J. Nat. Gas Sci. Eng. 24 (2015) 500–509. doi:10.1016/j.jngse.2015.03.022.

[12] J. Berger, S. Gasparin, D. Dutykh, N. Mendes, Accurate numerical simulation of moisture front in porous material, Build. Environ. 118 (2017) 211–224. doi:10.1016/j.buildenv.2017.03.016.

[13] C.R. Boardman, S. V. Glass, P.K. Lebow, Simple and accurate temperature correction for moisture pin calibrations in oriented strand board, Build. Environ. 112 (2017) 250–260. doi:10.1016/j.buildenv.2016.11.039.

[14] D. Mudarri, W.J.W. Fisk, Public health and economic impact of dampness and mold, Indoor Air. 17 (2007) 226–235. doi:10.1111/j.1600-0668.2007.00474.x.

[15] B.B. Mandelbrot, The fractal geometry of nature. Freeman and Company, New York, (1982).

[16] K. Falconer, Fractal Geometry: Mathematical Foundations and Applications, Wiley, New York, 2003.

[17] C. Atzeni, G. Pia, U. Sanna, N. Spanu, A fuzzy model for classifying mechanical properties of vesicular basalt used in prehistoric buildings, Mater. Charact. 59 (2008) 606–612. doi:10.1016/j.matchar.2007.05.001.

[18] G. Pia, L. Casnedi, U. Sanna, Porosity and pore size distribution influence on thermal conductivity of yttria-stabilized zirconia: Experimental findings and model predictions, Ceram. Int. 42 (2016) 5802–5809. doi:10.1016/j.ceramint.2015.12.122.

[19] G. Pia, Fluid flow in complex porous media: Experimental data and IFU model predictions for water vapour permeability, J. Nat. Gas Sci. Eng. 35 (2016) 283–290. doi:10.1016/j.jngse.2016.08.053.

[20] J. Carmeliet, S. Roels, Determination of the Isothermal Moisture Transport Properties of Porous Building Materials, J. Therm. Envel. Build. Sci. 24 (2001) 183–210. doi:10.1106/Y6T2-9LLP-04Y5-AN6T.

[21] R. Liu, Y. Jiang, B. Li, X. Wang, A fractal model for characterizing fluid flow in fractured rock masses based on randomly distributed rock fracture networks, Comput. Geotech. 65 (2015) 45–55. doi:10.1016/j.compgeo.2014.11.004.

[22] A. Jafari, T. Babadagli, Estimation of equivalent fracture network permeability using fractal and statistical network properties, J. Pet. Sci. Eng. 92–93 (2012) 110–123. doi:10.1016/j.petrol.2012.06.007.

[23] Q. Zheng, B. Yu, S. Wang, L. Luo, A diffusivity model for gas diffusion through fractal porous media, Chem. Eng. Sci. 68 (2012) 650–655. doi:10.1016/j.ces.2011.10.031.

[24] Q. Zheng, J. Xu, B. Yang, B. Yu, A fractal model for gaseous leak rates through contact surfaces under non-isothermal condition, Appl. Therm. Eng. 52 (2013) 54–61. doi:10.1016/j.applthermaleng.2012.11.011.

[25] G. Pia, E. Sassoni, E. Franzoni, U. Sanna, Predicting capillary absorption of porous stones by a procedure based on anintermingled fractal units model, Int. J. Eng. Sci. 82 (2014) 196–204. doi:10.1016/j.ijengsci.2014.05.013.

[26] G. Pia, C. Siligardi, L. Casnedi, U. Sanna, Pore size distribution and porosity influence on Sorptivity of ceramic tiles: From experimental data to fractal modeling, Ceram. Int. (2016). doi:http://dx.doi.org/10.1016/j.ceramint.2016.03.041.

[27] G. Pia, L. Casnedi, M. Ionta, U. Sanna, On the elastic deformation properties of porous ceramic materials obtained by pore-forming agent method, Ceram. Int. (2015). doi:10.1016/j.ceramint.2015.05.057.

[28] G. Pia, High porous yttria-stabilized zirconia with aligned pore channels: Morphology directionality influence on heat transfer, Ceram. Int. 42 (2016) 19–22. doi:10.1016/j.ceramint.2016.04.078.

[29] G. Pia, U. Sanna, An intermingled fractal units model to evaluate pore size distribution influence on thermal conductivity values in porous materials, Appl. Therm. Eng. 65 (2014) 330–336. doi:10.1016/j.applthermaleng.2014.01.037.

[30] UNI EN 15803 Conservation of cultural property - Test methods - Determination of water vapour permeability, (2009).

[31] E.A. Mason, A.P. Malinauskas, Gas transport in porous media: the dusty-gas model, Chemical Engineering Monographs 17, Elsevier, Amsterdam, 1983.

[32] V. Gitis, G. Rothemberg, Ceramic membranes: New opportunities and practical applications, Wiley-VCH, 2016.

[33] K. Keizer, R.J.R. Uhlhorn, R.J. Van Vuren, A.J. Burggraaf, Gas separation mechanisms in microuporous modified γ-Al2O3 membranes, J. Membr. Sci. Elsevier Sci. Publ. B.V. 39 (1988) 285–300.

[34] L. Martínez, F.J. Florido-Díaz, A. Hernández, P. Prádanos, Characterisation of three hydrophobic porous membranes used in membrane distillation Modelling and evaluation of their water vapour permeabilities, J. Memb. Sci. 203 (2002) 15–27. doi:10.1016/S0376-7388(01)00719-0.

[35] L.-Z. Zhang, A fractal model for gas permeation through porous membranes, Int. J. Heat

Mass Transf. 51 (2008) 5288–5295. doi:10.1016/j.ijheatmasstransfer.2008.03.008.

[36] S.W. Wheatcraft, S.W. Tyler, An explanation of scale-dependent dispersivity in heterogeneous aquifers using concepts of fractal geometry, Water Resour. Res. 24 (1988) 566–578. doi:10.1029/WR024i004p00566.

[37] B. Yu, P. Cheng, A fractal permeability model for bi-dispersed porous media, Int. J. Heat Mass Transf. 45 (2002) 2983–2993. doi:10.1016/S0017-9310(02)00014-5.

[38] B. Yu, Fractal Character for Tortuous Streamtubes in Porous Media, Chinese Phys. Lett. 22 (2005) 158–160. doi:10.1088/0256-307X/22/1/045.

[39] J. Comiti, M. Renaud, A new model for determining mean structure parameters of fixed beds from pressure drop measurements: application to beds packed with parallelepipedal particles, Chem. Eng. Sci. 44 (1989) 1539–1545.

[40] J. Cai, B. Yu, A Discussion of the Effect of Tortuosity on the Capillary Imbibition in Porous Media, Transp. Porous Media. 89 (2011) 251–263. doi:10.1007/s11242-011-9767-0.

[41] J. Cai, E. Perfect, C.-L. Cheng, X. Hu, Generalized Modeling of Spontaneous Imbibition Based on Hagen–Poiseuille Flow in Tortuous Capillaries with Variably Shaped Apertures, Langmuir. 30 (2014) 5142–5151. doi:10.1021/la5007204.

[42] J. Cai, L. Luo, R. Ye, X. Zeng, X. Hu, Recent advances on fractal modeling of permeability for fibrous porous media, Fractals. 23 (2015) 1540006. doi:10.1142/S0218348X1540006X.

[43] A.M. Attia, Effects of petrophysical rock properties on tortuosity factor, J. Pet. Sci. Eng. 48 (2005) 185–198. doi:10.1016/j.petrol.2005.06.012.

[44] I. Sevostianov, M. Shrestha, Cross-property connections between overall electric conductivity and fluid permeability of a random porous media with conducting sceleton, Int. J. Eng. Sci. 48 (2010) 1702–1708. doi:10.1016/j.ijengsci.2010.06.016.

[45] E. Sevostianova, B. Leinauer, I. Sevostianov, Quantitative characterization of the microstructure of a porous material in the context of tortuosity, Int. J. Eng. Sci. 48 (2010) 1693–1701. doi:10.1016/j.ijengsci.2010.06.017.

[46] X. Zhou, D. Derome, J. Carmeliet, Robust moisture reference year methodology for hygrothermal simulations, Build. Environ. 110 (2016) 23–35. doi:10.1016/j.buildenv.2016.09.021.

Figure captions

Fig. 1. Construction of the Sierpinski carpet with (a) 2 pores at first iteration and 7 iterating sub-squares at second iteration, and (b) 2 pores at first iteration, 4 iterating sub-squares and three unaffected solid sub-squares at second iteration.

Fig. 2. Schematic description of the modelling prediction of water vapour permeability. (a) Permeation experiments. (b) Porosimetric measurements and comparison between experimental and model pore size distributions. (c) Model estimation of water vapour permeability. (d) Comparison between model predictions and experimental findings.

Fig. 3. SEM micrographs showing the mesostructure of earth-based materials at (a) 500 μm and (b) 250 μm length scales.

Fig. 4. X-ray diffraction pattern of earth-based materials. Detected phases are suitably attributed.

Fig. 5. Comparison between experimental (solid line) and model (dotted line) porosimetric curves. Data refer to (a) E1-1, (b) E2-1, (c) E3-1 and (d) E4-1 samples.

Fig. 6. Water vapour absorption experiments. Mass variation, Δm, as a function of time, t. Data refer to E1 (□), E2 (○), E3 (Δ) and E4 (◊) samples. Best-fitted lines are shown.

Fig. 7. Comparison between experimental and model estimates of water vapour permeability. Comparison between water vapour permeability by experimental test and IFU calculations. Data refer to E1 (□), E2 (○), E3 (Δ) and E4 (◊) samples. The dotted line bisecting the quadrant indicates the condition of perfect agreement between experimental and modelling datasets.

Tab. 1. Composition (% by weight) of mixes used to prepare test specimens.

Tab. 2. Average microstructural characteristic of the earth sample E1-1, E2-1, E3-1 and E4-1. Total volume pore (P), porosity in the first range (P1), porosity in the second range (P2), porosity in the third range (P3) and medium pore radius (r_m).

Tab. 3. IFU input data to model E1-1, E2-1, E3-1 and E4-1. Fractal dimension (D_f), the maximum (R_{max}) and minimum ray (R_{min}), the number of iterations, the number of solid forever squares for each base units (Sierpinski carpet), the number of B base units (n_B), the filled surface used to build the IFU.

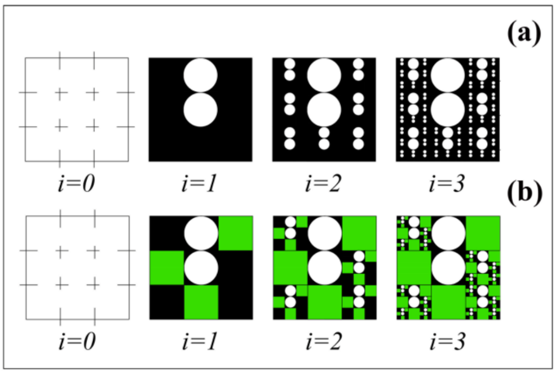

Fig. 1

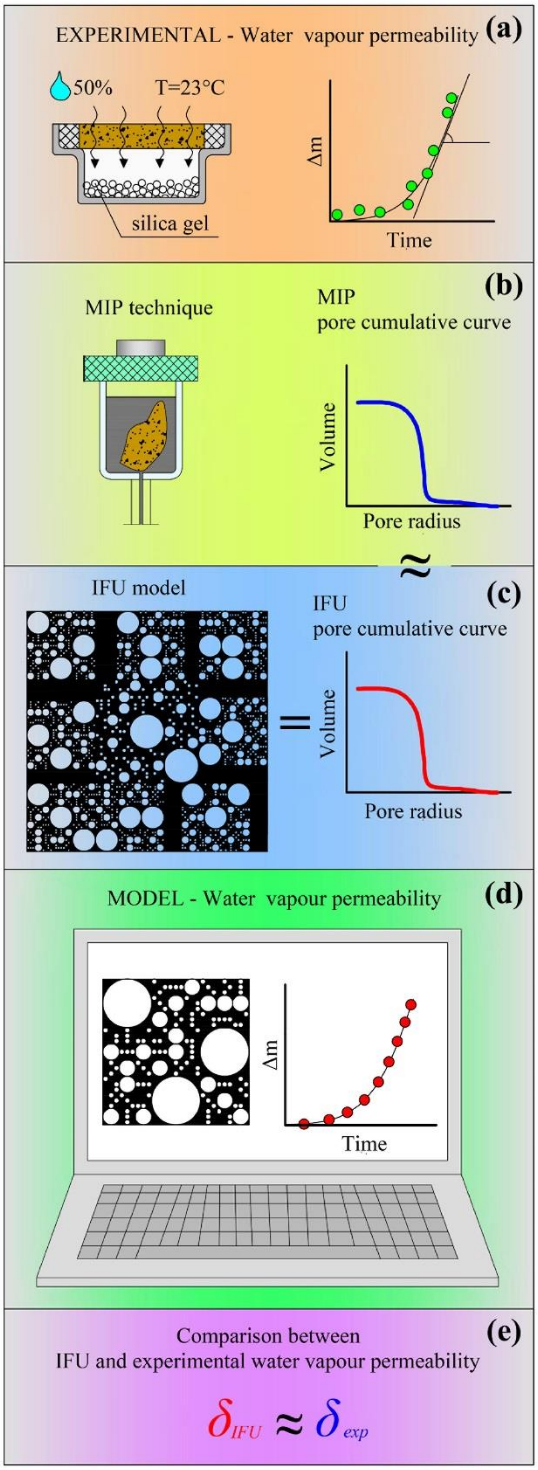
EXPERIMENTAL - Water vapour permeability
(a)
50%
T=23°C
silica gel
Δm
Time
(b)
MIP technique
MIP
pore cumulative curve
Volume
Pore radius
≈
IFU model
(c)
IFU
pore cumulative curve
=
Volume
Pore radius
MODEL - Water vapour permeability
(d)
Δm
Time
Comparison between
IFU and experimental water vapour permeability
(e)
δ_IFU ≈ δ_exp

Fig. 2

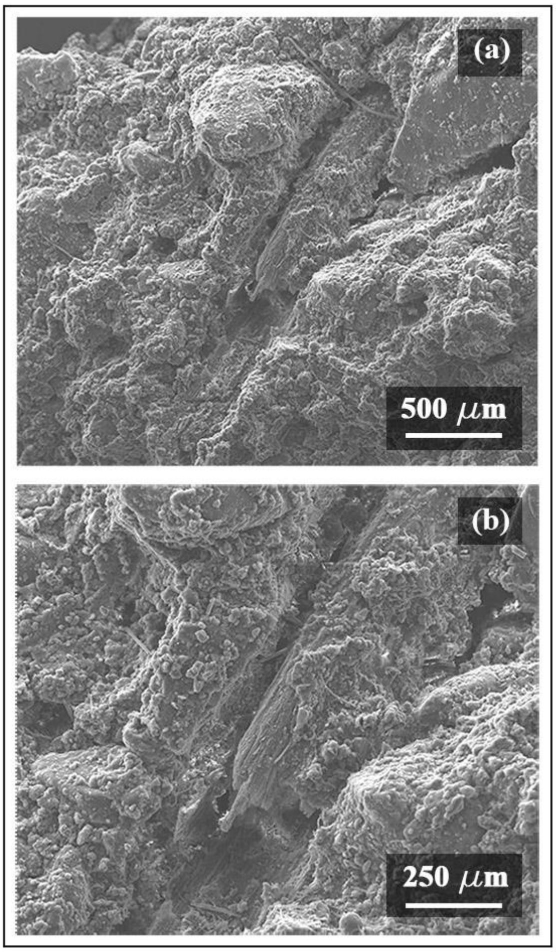

Fig. 3

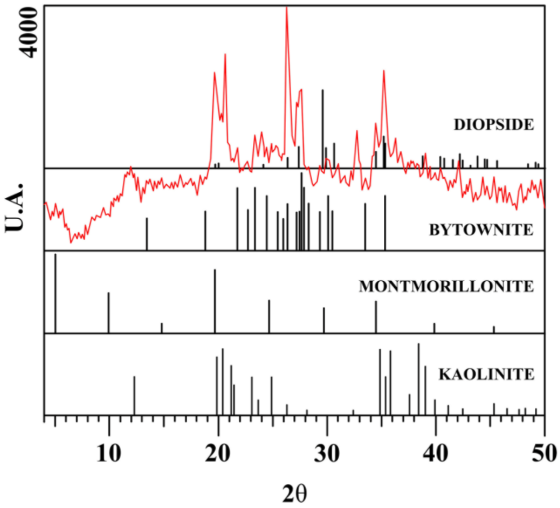
4000
U.A.
DIOPSIDE
BYTOWNITE
MONTMORILLONITE
KAOLINITE
10
20
30
40
50
2θ

Fig. 4

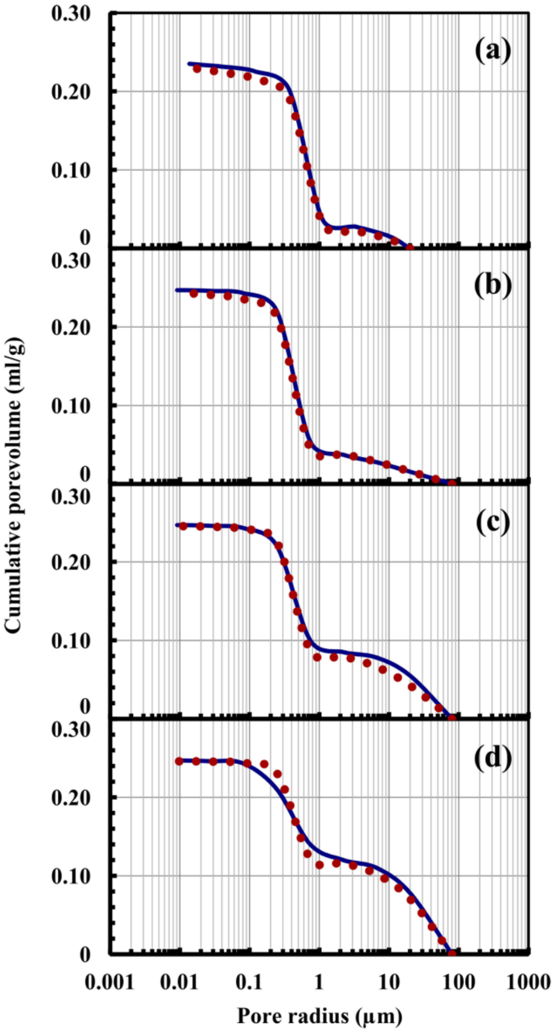
(a)
(b)
(c)
(d)
0.30
0.20
0.10
0
Cumulative porevolume (ml/g)
0.001
0.01
0.1
1
10
100
1000
Pore radius (µm)

Fig. 5

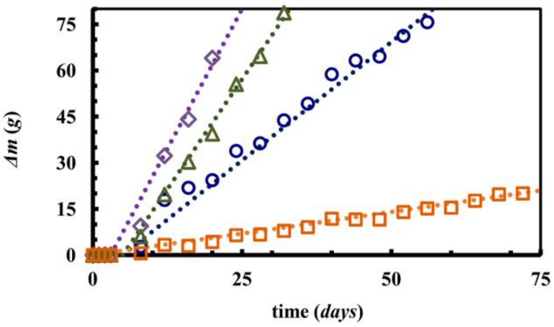

Fig. 6

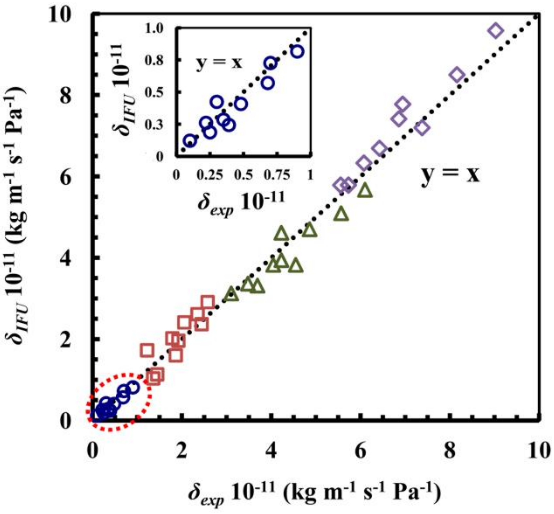

δ_{IFU} 10^{-11} (kg m^{-1} s^{-1} Pa^{-1})
δ_{exp} 10^{-11} (kg m^{-1} s^{-1} Pa^{-1})
0
2
4
6
8
10
y = x
1.0
0.8
0.5
0.3
0
0.25
0.5
0.75
1
δ_{IFU} 10^{-11}
δ_{exp} 10^{-11}

Fig. 7

Tab. 1. Composition (% by weight) of mixes used to prepare test specimens.

System	Soil	Water	Sand	Straw
E1	75	20	--	5
E2	65	15	15	5
E3	55	13	27	5
E4	45	12	38	5

Tab. 2. Average microstructural characteristic of the earth sample E1-1, E2-1, E3-1 and E4-1. Total volume pore (P), porosity in the first range (P1), porosity in the second range (P2), porosity in the third range (P3) and medium pore radius (r_m).

Sample	P (%)	P_1 (%) 100 ÷ 1.10 μm	P_2 (%) 1.10 ÷ 0.1 μm	P_3 (%) 0.1 ÷ 0.009 μm	r_m (μm)
E1-1	12.98	2.00	10.19	0.54	0.74
E2-1	18.02	2.71	15.70	0.29	0.49
E3-1	17.81	6.22	11.56	0.29	0.49
E4-1	22.15	10.73	11.00	0.36	0.49

Tab. 3. IFU input data to model E1-1, E2-1, E3-1 and E4-1. Fractal dimension (D_f), the maximum (R_{max}) and minimum ray (R_{min}), the number of iterations, the number of solid forever squares for each base units (Sierpinski carpet), the number of B base units (n_B), the filled surface used to build the IFU.

		E1-1	E2-1	E3-1	E4-1
Unit A	D_f	1.89	1.77	1.77	1.77
	n	1	1	1	1
	R_{max} *(µm)*	10	20	20	20
	Iteration	6	7	7	7
	R_{min} *(µm)*	0.014	0.009	0.009	0.009
	Solid forever	0	0	2	3
Unit B	D_f	1.77	1.77	1.77	1.77
	n	4642	66593	20623	9828
	R_{max} *(µm)*	0.37	0.25	0.25	0.25
	Iteration	3	3	3	3
	R_{min} *(µm)*	0.014	0.009	0.009	0.009
	Solid forever	6	6	6	6
	Filled surface (μm^2)	$3.67\cdot10^4$	$1.16\cdot10^5$	$4.31\cdot10^4$	$1.47\cdot10^4$